

Modeling the Interface between Lithium Metal and Its Native Oxide

Jeffrey S. Lowe and Donald J. Siegel*

Cite This: *ACS Appl. Mater. Interfaces* 2020, 12, 46015–46026

Read Online

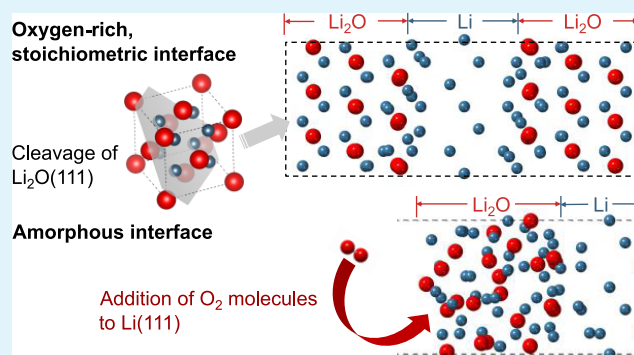
ACCESS |

Metrics & More

Article Recommendations

ABSTRACT: Owing to their high theoretical capacities, batteries that employ lithium (Li) metal as the negative electrode are attractive technologies for next-generation energy storage. However, the successful implementation of lithium metal batteries is limited by several factors, many of which can be traced to an incomplete understanding of surface phenomena involving the Li anode. Here, first-principles calculations are used to characterize the native oxide layer on Li, including several properties associated with the Li/lithium oxide (Li_2O) interface. Multiple interface models are examined; the models account for differing interface (chemical) terminations and degrees of atomic ordering (i.e., crystalline vs amorphous). The interfacial energy, formation energy, and strain energies are predicted for these models. The amorphous interface yields the lowest interfacial formation energy, suggesting that it is the most probable model under equilibrium conditions. The work of adhesion is evaluated for the crystalline interfaces, and it is found that the O-terminated interface exhibits a work of adhesion more than 30 times larger than that of the Li-terminated model, implying that Li will strongly wet an oxygen-rich Li_2O surface. The electronic structure of the interfaces is characterized using Voronoi charge analysis and shifts in the Li 1s binding energies. The width of the Li/ Li_2O interface, as determined by deviations from bulklike charges and binding energies, extends beyond the region exhibiting interfacial structural distortions. Finally, the transport of Li ions through the amorphous oxide is quantified using ab initio molecular dynamics. Facile transport of Li^+ through the native oxide is observed. Thus, increasing the percentage of amorphous Li_2O in the solid electrolyte interphase may be beneficial for battery performance. In total, the phenomena quantified here will aid in the optimization of batteries that employ high-capacity Li metal anodes.

KEYWORDS: batteries, energy storage, Li-metal anode, oxidation, amorphous interface, diffusivity



INTRODUCTION

Lithium metal batteries (LMBs) that employ a metallic lithium (Li) anode are an attractive technology for next-generation battery architectures. Compared to the current Li-ion technology, which uses a graphite-based anode, LMBs theoretically can increase specific capacities by an order of magnitude: 370 mAh/g graphite vs 3860 mAh/g Li metal.¹ However, the successful implementation of LMBs is limited by a number of factors, many of which can be traced to an incomplete understanding of the structure and chemistry of the Li anode surface.

Reactions between this surface and the adjacent electrolyte can result in the formation of a solid electrolyte interphase (SEI). Ideally, SEI formation should be self-limiting, i.e., SEI growth and electrolyte decomposition will cease once the SEI reaches a critical thickness. Nevertheless, in LMBs, electrolyte decomposition can occur continuously with conventional carbonate solvents, leading to electrolyte depletion.^{2–6} Even with solvents more suitable to use in LMBs, such as 1,3-dioxolane (DOL), electrolyte decomposition may occur.⁶ Electrolyte decomposition products, as evidenced by the

components of the SEI, vary widely based on the composition of the electrolyte.¹

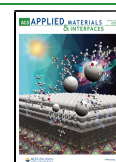
In addition, Li-ion transport through the SEI can be a concern.⁷ Efficient battery operation requires that Li ions be able to migrate across the SEI with limited resistance. Nonetheless, many SEIs formed in LMBs have low ionic conductivity.^{8–11}

Finally, during charging, it is known that Li can plate inhomogeneously on the anode surface. This can lead to the formation of “dendrites” that short-circuit the cell. An extensive body of work has attempted to eliminate this failure mode through the application of various protection strategies. Typically, these focus on altering the surface of the Li anode so as to control the structure of the SEI. An incomplete list of

Received: July 9, 2020

Accepted: September 15, 2020

Published: September 15, 2020



strategies that have been explored includes the following: use of two-dimensional membranes,^{12,13} application of coatings via atomic layer deposition,^{14–16} film-forming electrolyte additives,^{9,17} electrode modification,¹⁸ or through using a solid electrolyte.¹⁹ While these strategies have demonstrated improved performance of LMBs, to our knowledge, none are yet capable of enabling a practical, high-capacity, rechargeable LMB.

As a step toward a viable LMB, the present study aims to clarify the chemistry and structure of the Li metal surface. More specifically, we focus on the properties of its native oxide layer, Li₂O, and on the interface between this oxide and the underlying Li metal. It is well known that a Li₂O native oxide layer is present on the Li surface, even when Li is fabricated/handled in an oxygen-poor environment.²⁰ Consequently, Li₂O is typically found as the innermost component of the SEI and appears to be the one component of the SEI that is universal across all electrolyte chemistries.

Many studies attribute the cycling behavior of LMBs to the oxide layer on the Li metal surface.^{5,17,18,21–23} For example, Adams et al.¹⁷ showed that adding LiNO₃ to a DOL/dimethoxyethane (DME) electrolyte of a Li–S cell led to improvements in Coulombic efficiency and cycle life. This improved behavior was attributed to the increased presence of Li₂O within the SEI and on the surface of Li metal, which was suggested to inhibit the decomposition of salt and solvent species in the electrolyte. Since the Li₂O present in the SEI was suggested to form due to oxidation of Li by the LiNO₃ additive, native Li₂O may exhibit similar (beneficial) behavior. Cui and co-workers used cryogenic transmission electron microscopy (cryo-TEM) to characterize the SEI formed on a Li metal anode in the presence of carbonate-based electrolytes that contained either fluoroethylene carbonate (FEC)⁵ or LiNO₃²¹ additives. When the additives were present, the SEI exhibited an inner, amorphous polymer layer and an outer, ordered Li₂O layer. In the absence of additives, the SEI primarily consisted of an amorphous polymer layer, with some embedded pockets of crystalline Li₂O and Li₂CO₃.

Previous computational studies have developed models for the Li/Li₂O interface. Lepley and Holzwarth created two crystalline Li/Li₂O models and computed the interfacial and strain energy in both systems.²⁴ Koch et al. conducted a gas adsorption and surface incorporation simulation on three low-index Li surfaces with various atmospheric gases, including O₂.²⁵ The structural, electronic, and elastic properties of the various interfaces were analyzed.

The present study expands upon these investigations by characterizing several models of the interface between Li metal and its native oxide in the context of batteries that employ Li metal anodes. Multiple interface models are constructed, accounting for differing (chemical) interface terminations and atomic ordering (crystalline vs amorphous). For all models, the interfacial energy, formation energy, and strain energies are computed. The amorphous model displays the lowest interfacial formation energy, suggesting that it is the most representative model under standard conditions. The work of adhesion is evaluated for oxygen-rich (O-terminated) and stoichiometric (Li-terminated) crystalline interfaces. The oxygen-rich interface exhibits a work of adhesion more than 30 times larger than the stoichiometric case, implying that Li will strongly wet a surface with exposed O atoms.

In addition, the electronic structures of the crystalline interfaces and of the amorphous interface are evaluated with

Voronoi charge analysis and computed shifts in Li 1s core-level electron binding energies. Considering deviations in atomic charges and electron binding energies from bulk Li and Li₂O, the width of the Li/Li₂O interface is shown to extend beyond the region near the interface, where the atomic structure deviates from that in bulk. Finally, the Li⁺ transport properties of the amorphous interface model are assessed with ab initio molecular dynamics (AIMD) simulations at a range of temperatures. Facile transport of Li⁺ through the native oxide is observed. Thus, increasing the proportion of amorphous Li₂O in the SEI may improve Li⁺ transport. Taken together, this work clarifies the structural, transport, and mechanical properties of the Li metal/native oxide interface at the atomic scale.

METHODOLOGY

All calculations were performed using density functional theory (DFT), as implemented in the Vienna Ab initio Simulation Package (VASP).^{26–29} The exchange–correlation energy was described using the functional of Perdew, Burke, and Ernzerhof (PBE),³⁰ and the projector-augmented wave method was used to describe interactions between core and valence electrons.^{31,32} A 440 eV plane-wave energy cutoff was used and the force minimization criterion was set at 0.04 eV/Å. The *k*-point mesh was specified as 2 × 2 × 1 for total energy calculations and 6 × 6 × 1 for core-level binding energy shift (CLS) calculations.

Crystalline Interfaces. A crystalline interface of the Li/Li₂O interface was constructed using the lowest energy Li₂O surface (111), as determined in a previous study.³³ The Li surface interfaced with Li₂O was selected as the (111) facet, since this surface results in the lowest interfacial strain with Li₂O(111) among the low-index surfaces of Li [(100), (110), and (111)], and the surface energy differences between these facets are relatively small.³⁴ For the Li₂O slab, both a Li-terminated and an O-terminated slab were investigated. The former slab maintains the stoichiometry of bulk Li₂O, while the latter has an excess of oxygen (oxygen-rich). In both cases, the Li/Li₂O interface was constructed by straining a 3 × 3 Li₂O(111) supercell by 1.12% to match a 2 × 2 Li(111) supercell. The interface supercell consisted of two equivalent interfaces having dimensions of 9.73 Å × 9.73 Å. In the oxygen-rich model, a stacking fault was created in the bulk region of Li₂O to create two, symmetry-equivalent interfaces. The stacking fault energy was removed (via subtraction) when evaluating the thermodynamic properties of this interface.

The relaxed interfacial structure was determined by minimizing the total energy with respect to rigid translations in all three directions. This was achieved by first calculating the γ surface; specifically, the Li₂O slab was rigidly translated in directions parallel to the interface so as to map the energy as a function of translation. Then, using the lowest energy structure on the γ surface as the starting configuration, the universal binding energy (UBER)^{35–38} curve was calculated by incrementally modifying the distance between the two slabs in the direction perpendicular to the interface. Finally, adopting the lowest energy structure from the UBER as input, the entire interface cell was then relaxed by allowing modifications to both the atom positions and the lattice parameters. The resulting fully relaxed structure was subsequently used for computing thermodynamic properties.

Three interfacial properties were evaluated for the various models of the Li/Li₂O interface: the interface formation

energy, E_F , the interfacial energy, γ , and the interfacial strain energy, ζ . E_F describes the energy required (on a per atom basis) to form the Li/Li₂O interface, including strain effects, relative to unstrained bulk Li and Li₂O. Interfaces that minimize E_F are the most probable under equilibrium conditions. The interfacial energy, γ , differs from the formation energy in that γ omits strain contributions. γ is a measure of the relative bonding strength at an interface: γ values less than (greater than) zero imply that interfacial bonds are on average stronger (weaker) than in the separate interfacial components. Finally, the strain energy, ζ , is the energy needed to deform one or both of the interfacial components into registry at the interface.

For the stoichiometric interface, the formation energy of the Li/Li₂O interface (per atom), E_F , is given by³⁹

$$\frac{E_F}{N} = E_{\text{Li/Li}_2\text{O}} - n_{\text{Li}}^{\text{Li(BCC)}} \mu_{\text{Li}}^{\text{Li(BCC)}} - n_{\text{Li}_2\text{O}} E_{\text{Li}_2\text{O}} \quad (1)$$

where $E_{\text{Li/Li}_2\text{O}}$ is the energy of the relaxed interface cell, $n_{\text{Li}}^{\text{Li(BCC)}}$ is the number of Li atoms in the Li slab, $\mu_{\text{Li}}^{\text{Li(BCC)}}$ is the chemical potential of Li in bulk Li metal, $n_{\text{Li}_2\text{O}}$ is the number of formula units of Li₂O in the Li₂O slab, $E_{\text{Li}_2\text{O}}$ is the bulk energy of one formula unit of Li₂O, and N is the total number of atoms in the interface cell. The interfacial energy, γ , was then determined using the method described by Wolverton and co-workers.³⁹ Based on this method, the interfacial energy for the stoichiometric system was computed as

$$\gamma = \frac{E_{\text{Li/Li}_2\text{O}} - n_{\text{Li}}^{\text{Li(BCC)}} \mu_{\text{Li}}^{\text{Li(BCC)}} - n_{\text{Li}_2\text{O}} E_{\text{Li}_2\text{O(c)}}}{2A} \quad (2)$$

where $E_{\text{Li}_2\text{O(c)}}$ is the energy of a formula unit of bulk Li₂O in which the **a** and **b** lattice vectors (which are parallel to the interface plane) have been strained to match their values in the interface cell. In this case, only the **c** lattice vector, corresponding to the direction normal to the interface, is relaxed. $2A$ is the interfacial area. Note that in our calculations the Li₂O slab has been strained to match the lattice parameters of the Li slab. Therefore, the Li slab does not experience strain. The strain energy (per atom), ζ , can be calculated as the difference of the formation and interfacial energies³⁹

$$\zeta = \frac{1}{N} (E_F - 2A\gamma) \quad (3)$$

For the interface involving the nonstoichiometric oxygen-rich Li₂O slab, the ratio of Li to O atoms in the Li₂O slab is not equal to 2:1; hence, the equation for the formation energy includes the chemical potentials of oxygen and lithium⁴⁰

$$\frac{E_F}{N} = E_{\text{Li/Li}_2\text{O}} - n_{\text{Li}}^{\text{Li(BCC)}} \mu_{\text{Li}}^{\text{Li(BCC)}} - n_{\text{Li}}^{\text{Li}_2\text{O}} \mu_{\text{Li}}^{\text{Li}_2\text{O}} - n_{\text{O}} \mu_{\text{O}}^{\text{Li}_2\text{O}} \quad (4)$$

where $n_{\text{Li}}^{\text{Li}_2\text{O}}$ is the number of Li atoms in the Li₂O slab, $\mu_{\text{Li}}^{\text{Li}_2\text{O}}$ is the chemical potential of Li in bulk Li₂O, n_{O} is the number of oxygen atoms in the Li₂O slab, and $\mu_{\text{O}}^{\text{Li}_2\text{O}}$ is the chemical potential of oxygen in bulk Li₂O. In eq 4, there are two unknown terms, $\mu_{\text{Li}}^{\text{Li}_2\text{O}}$ and $\mu_{\text{O}}^{\text{Li}_2\text{O}}$. However, these two terms can be related through the energy of a formula unit of bulk Li₂O as

$$E_{\text{Li}_2\text{O}} = \mu_{\text{O}}^{\text{Li}_2\text{O}} + 2\mu_{\text{Li}}^{\text{Li}_2\text{O}} \quad (5)$$

Thus, only one of $\mu_{\text{Li}}^{\text{Li}_2\text{O}}$ and $\mu_{\text{O}}^{\text{Li}_2\text{O}}$ is an independent variable. We computed the formation energy by specifying the values of

these chemical potentials corresponding to two extremes, representing two distinct equilibrium conditions. In the first case, $\mu_{\text{Li}}^{\text{Li}_2\text{O}}$ is set to its value in bulk Li ($\mu_{\text{Li}}^{\text{Li(BCC)}}$). In the second case, $\mu_{\text{O}}^{\text{Li}_2\text{O}}$ is set to its value in oxygen gas ($\mu_{\text{O}}^{\text{O}_2(\text{g})}$). Substituting eq 5 for the last two terms in eq 4 gives

Equilibrium condition 1: $\mu_{\text{Li}}^{\text{Li}_2\text{O}} = \mu_{\text{Li}}^{\text{Li(BCC)}}$

$$\frac{E_F}{N} = E_{\text{Li/Li}_2\text{O}} - n_{\text{Li}}^{\text{Li(BCC)}} \mu_{\text{Li}}^{\text{Li(BCC)}} - n_{\text{Li}_2\text{O}} \mu_{\text{Li}}^{\text{Li(BCC)}} - n_{\text{O}} (E_{\text{Li}_2\text{O}} - 2\mu_{\text{Li}}^{\text{Li(BCC)}}) \quad (6)$$

Equilibrium condition 2: $\mu_{\text{O}}^{\text{Li}_2\text{O}} = \mu_{\text{O}}^{\text{O}_2(\text{g})}$

$$\frac{E_F}{N} = E_{\text{Li/Li}_2\text{O}} - n_{\text{Li}}^{\text{Li(BCC)}} \mu_{\text{Li}}^{\text{Li(BCC)}} - n_{\text{Li}_2\text{O}} \left(\frac{1}{2} E_{\text{Li}_2\text{O}} - \frac{1}{2} \mu_{\text{O}}^{\text{O}_2(\text{g})} \right) - n_{\text{O}} \mu_{\text{O}}^{\text{O}_2(\text{g})} \quad (7)$$

Subsequently, the interfacial and strain energies for the oxygen-rich interface were determined using an approach identical to that used for the stoichiometric interface. As mentioned above, a stacking fault was introduced in the oxygen-rich model to create two identical interfaces; the energy contribution of this stacking fault was removed from the energy of the fully relaxed cell by comparing with the bulk energy of Li₂O.

Work of Adhesion. The work of adhesion, W_{ad} , was computed using³⁶

$$W_{\text{ad}} = \sigma_{\text{Li}} + \sigma_{\text{Li}_2\text{O}} - \gamma_{\text{Li/Li}_2\text{O}} \quad (8)$$

where σ_{Li} and $\sigma_{\text{Li}_2\text{O}}$ are the surface energies of Li and Li₂O, and $\gamma_{\text{Li/Li}_2\text{O}}$ is the energy of the interface formed when Li and Li₂O are in contact with one another. The work of adhesion was computed for both interface terminations as the energy difference between configurations in which the two slabs were roughly 10 Å apart ($\sigma_{\text{Li}} + \sigma_{\text{Li}_2\text{O}}$) and when they were in contact ($\gamma_{\text{Li/Li}_2\text{O}}$). The configuration used to calculate $\gamma_{\text{Li/Li}_2\text{O}}$ was taken to be the one which minimized the energy due to translation in all three spatial directions. Equation 8 was used to obtain both the unrelaxed (all atoms fixed) and relaxed work of adhesion.

Amorphous Interface. An amorphous model of the Li₂O/Li interface was created starting from the same 2×2 Li(111) slab as used in the crystalline interface. Then, using a procedure similar to that used to generate an amorphous oxidized layer on TiN(100),⁴¹ several O₂ molecules were sequentially added (at rest) 3.0 Å above the Li(111) surface at the same position in the simulation cell. The system was evolved using 4 ps of AIMD in the canonical (NVT) ensemble at 300 K following the addition of each O₂ molecule. The bottom three Li layers of the Li slab were fixed at their bulk positions. A time step of 1 fs was used and a Nosé thermostat⁴² was employed with a mass of ~ 50 amu·Å² (SMASS = 0.30). In total, 11 O₂ molecules were added, amounting to a surface coverage of roughly two monolayers of crystalline Li₂O. Between the addition of six and seven O₂ molecules, five additional Li layers were added to the bottom half of the Li slab to allow for more O₂ molecules to be added to the top half of the simulation cell, while maintaining a Li metal substrate. Following the incorporation of the final O₂ molecule, an additional 10 ps AIMD simulation at 300 K was performed.

This was followed by a 4 ps annealing run at 600 K and a 4 ps cooling run again at 300 K.

Charge Analysis. Charge analysis was performed following the incorporation of each O₂ molecule into the Li surface (and the subsequent 4 ps AIMD simulation) for the amorphous interface and on the relaxed, crystalline systems. Charge transfer was analyzed using the Voronoi charge partitioning scheme.^{43–46} In comparison to Bader charge partitioning, which divides charges based on minima in the charge density profile, Voronoi partitioning assigns charges based on geometrical considerations (Voronoi polyhedra). This choice was made because a Bader analysis assigned very large Bader volumes to Li atoms near the surface, resulting in unphysical charges on these atoms.

Core-Level Binding Energy Shifts. Shifts in the Li 1s core-level electron binding energies were calculated using the final state approach.^{47,48} This analysis, which can be compared to the binding energy of an electron obtained from X-ray photoelectron spectroscopy (XPS) measurements, enables one to distinguish between different electronic environments experienced by individual Li atoms (i.e., Li 1s electrons in Li metal vs Li 1s electrons in Li₂O). This allows one to differentiate between oxide, metallic, and transition regions within the models, which, in turn, govern the properties of the interface.

In the final state approach, one electron is excited from the core to the valence band; the energy difference between the excited state and the ground state is used to obtain the electron's binding energy⁴⁷

$$BE_i^{\text{FS}} = E(n_i - 1) - E(n_i) \quad (9)$$

where $E(n_i - 1)$ is the energy of the system in the excited state and $E(n_i)$ is the energy of the system in the ground state. In the final state approximation, the valence electrons are allowed to relax in the excited state configuration, which results in a screening of the core hole. It is well known that the calculation of absolute binding energies is problematic for ground-state techniques such as DFT.⁴⁸ Nevertheless, shifts in the core-level binding energies (CLSs) are typically reliable and can be expressed as⁴⁷

$$E_{\text{CLS}} = BE - BE^{\text{ref}} \quad (10)$$

Here, BE and BE^{ref} are the electron binding energies as computed with eq 9 for the atom of interest and for a reference atom, respectively. To validate this approach, the Li 1s CLSs of various bulk materials containing Li were computed using the final state approach and compared to experiments (Figure 1). The experimental data set was chosen to match that presented in the work by Wood and Teeter,⁴⁹ which demonstrated a rigorous approach for identifying various Li-containing phases using XPS measurements. In line with that study, a minimum of seven experimental measurements from multiple sources were used for each material; the error bar in Figure 1 corresponds to the standard deviation of the data. The binding energies were all referenced to Li₂CO₃ since that material had the least amount of deviation in the experimental measurements. As shown in the figure, the computed values are in reasonable agreement with the experimental data. Only the computed value for LiOH falls outside of the range of the experimental data and does so by a small amount, ~0.3 eV. Further, the current study only considers the CLSs for Li and Li₂O, for which there is excellent agreement between the

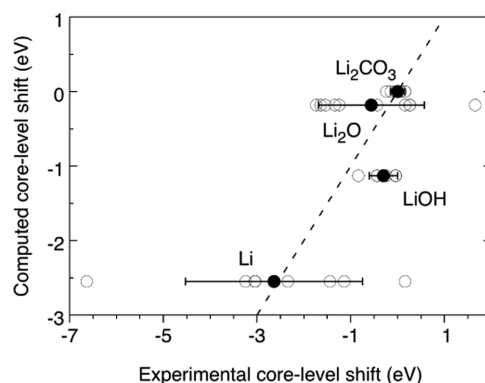


Figure 1. Comparison between the computed Li 1s core-level binding energy shift (vertical axis) and the experimental binding energy shift (horizontal axis) for several Li-based compounds. All shifts are relative to Li₂CO₃. The dashed line represents perfect agreement between computation and experiment. Error bars depict the standard deviation of the experimental data. Individual experimental data points are given by open circles, and average values are indicated by closed circles.^{64–83}

theory and experiment. As such, this approach is expected to reliably predict experimental core-level shifts across the diverse Li-containing systems considered in this study. Calculations were performed for each amorphous model geometry (i.e., following the incorporation of each O₂ molecule) and in the crystalline systems.

Li-Ion Diffusivities. The diffusivities of Li ions were computed from three sets of 40 ps AIMD simulations in the canonical ensemble. This analysis was performed on the amorphous model with the thickest oxide layer at $T = 900, 1000, 1100,$ and 1200 K. These high temperatures were required to achieve sufficient sampling of the long-range diffusion of Li⁺. The time step was set to be no greater than 3 fs. The mean-squared displacement (MSD) of Li ions was calculated (with the exception of the bottom three Li layers, which were fixed at their bulk positions) following the procedure outlined by He et al.⁵⁰ In this procedure, the MSD is computed with respect to δt , where δt is a time window that is shifted across the entire simulation time. For example, for $\delta t = 1$ ps, the MSD would be the average squared displacement of all Li ions in the time intervals 0–1, 1–2, ..., 39–40 ps. Therefore, over the course of a 40 ps simulation, several time intervals are sampled, with a larger number of samples included as δt is reduced. This procedure results in an improved estimate of the MSD compared to the traditional procedure (where only a single time interval is used).

For each 40 ps simulation, the slope of the MSD curve in the diffusional displacement regime was used to calculate the diffusion coefficient using the Einstein relation⁵⁰

$$D = \frac{\text{MSD}(\delta t)}{2d\delta t} + D_{\text{offset}} \quad (11)$$

where d is the dimensionality of the system ($d = 3$) and D_{offset} is the y -intercept. This relation only holds for the diffusional displacement regime, where a linear relationship between δt and MSD is observed. The linear regime used for determining the diffusion coefficient was taken to be $1 \text{ ps} < \delta t < 10 \text{ ps}$. Below this interval, the MSD curve was nonlinear; above this interval, the deviation in the computed diffusion coefficients was large due to insufficient sampling. The diffusion coefficients were used to generate an Arrhenius plot from

which the activation energy for Li-ion diffusion was determined.

RESULTS AND DISCUSSION

The structures of the various Li/Li₂O interface models constructed in this work (both crystalline and amorphous) are depicted in Figure 2. As expected, the amorphous model,

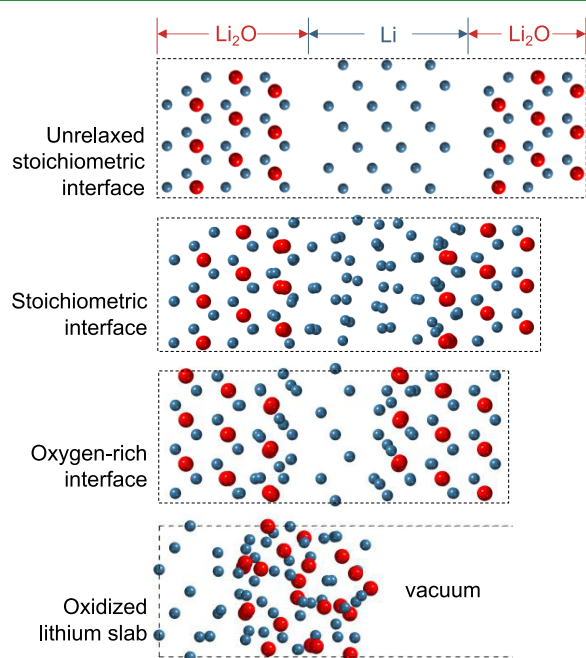


Figure 2. Structures of the unrelaxed stoichiometric, the relaxed stoichiometric, the relaxed oxygen-rich, and the oxidized lithium slab (11 O₂ atoms incorporated) interfaces. Li and O atoms are colored blue and red, respectively.

identified as the “oxidized Li slab” in Figure 2, exhibits a more disordered structure than does the other two models. The more ordered appearance of the crystalline interfaces results from the fact that these systems were constructed by interfacing two crystalline slabs. Additional details regarding the various models are described below.

Crystalline Interface. Two models for the crystalline Li/Li₂O interface were examined: one with a stoichiometric Li₂O surface and the other with an oxygen-rich Li₂O surface. Using eqs 1–7, the formation, interfacial, and strain energies were computed for both models; these data are summarized in Table 1. Independent of the equilibrium conditions, the oxygen-rich interfacial termination exhibits more favorable formation and interfacial energies relative to the stoichiometric interface. Formation energies range from −5.81 to −34.7 kJ/

mol and interfacial energies range from −1.11 to −6.44 J/m² for the oxygen-rich model. These values are 3.76 kJ/mol and 0.730 J/m², respectively, for the stoichiometric model. Both formation and interfacial energies are negative in the oxygen-rich model, which shows that the Li/Li₂O interface is lower in energy than an equivalent amount of (isolated) bulk Li and Li₂O. This behavior implies the presence of strong interfacial bonding for this termination.

Lepley and Holzwarth also assessed interfacial thermodynamics for two crystalline Li/Li₂O interfaces with DFT.²⁴ The authors obtained interfacial energies of 0.417 and 0.481 J/m² for Li(110)/Li₂O(110) and Li/Li₂O(110), respectively. In the latter system, the Li layer consisted of an orthorhombic structure matched to the Li positions in Li₂O. These values more closely match the interfacial energy in the stoichiometric model than in the oxygen-rich model. This similarity may be due to the fact that both the stoichiometric model and Li₂O(110) include lithium atoms in the outermost layer. Because the models examined by Lepley and Holzwarth employed different surface facets and exchange–correlation functional (local-density approximation (LDA) instead of the generalized gradient approximation (GGA)), quantitative differences with our results are expected.

Additionally, in all crystalline interfaces, the contribution from coherency strain energy (i.e., the strain required to match the surface lattice constants at the interface) is small (Table 1). For the stoichiometric system, the calculated strain of 0.097 kJ/mol is 2.6% of the formation energy. For the oxygen-rich system, the strain energy is 0.176 kJ/mol, which is between 0.5 and 3.0% of the formation energy, depending on the equilibrium condition adopted (discussed below). For comparison, another DFT study by Liu et al.³⁴ reported that strain energy contributions to the formation energies for Li/LiF and Li/Li₂CO₃ interfaces ranged from 0.2 to 11.7%. Thus, the computed values for the Li/Li₂O interfaces examined here fall within the lower end of this range.

Figure 3 plots the interfacial energies of the crystalline interface models as a function of oxygen chemical potential. Here, the *x*-axis represents the change in the chemical potential of oxygen, Δμ_O, with respect to that of oxygen gas, O₂. The lower and upper bounds represent equilibrium conditions 1 and 2 (eqs 6 and 7), respectively. Figure 3 shows that the oxygen-rich system is always lower in energy than the stoichiometric system. This behavior can be attributed to a strong interaction between the O-terminated, oxygen-rich Li₂O surface slab, and the Li metal slab. The preference for an O-terminated interface at metal/oxide junctions has been observed in previous DFT studies. For example, Zhang and Smith found that in the Nb/Al₂O₃ system an O-terminated interface was preferred over an Al-terminated alternative over the majority of oxygen chemical potentials considered.⁴⁰ In

Table 1. Calculated Properties for Li/Li₂O Interfaces^a

model	E_f (kJ/mol)	γ (J/m ²)	ζ (kJ/mol)	unrelaxed W_{ad} (J/m ²)	relaxed W_{ad} (J/m ²)	contact angle (deg)
stoichiometric	3.76	0.730	0.097	0.08	0.18	132
O-rich (Li eqm.)	−5.81	−1.11	0.176	4.28	6.69	~0
O-rich (O eqm.)	−34.7	−6.44	0.176	4.28	6.69	~0
amorphous (Li eqm.)	−18.1	−3.03				
amorphous (O eqm.)	−46.3	−7.71				

^a E_f is the formation energy, γ is the interfacial energy, ζ is the strain energy, W_{ad} is the work of adhesion, Li eqm. represents equilibrium condition 1 ($\mu_{Li}^{Li_2O} = \mu_{Li}^{Li(BCC)}$), and O eqm. represents equilibrium condition 2 ($\mu_{O}^{Li_2O} = \mu_{O}^{O_2(g)}$).

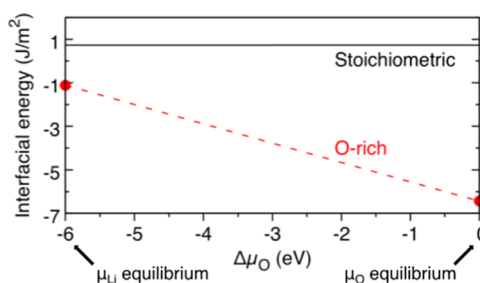


Figure 3. Interfacial energies for Li/Li₂O crystalline interfaces with oxygen-rich (red, dashed line) and stoichiometric (black, solid line) Li₂O surfaces. The *x*-axis is the change in oxygen chemical potential with respect to its value in O₂ gas. The *x*-axis range (−6.00 eV) is set by the DFT-computed formation energy of bulk Li₂O; its lower bound represents equilibrium condition 1 ($\mu_{\text{Li}}^{\text{Li}_2\text{O}} = \mu_{\text{Li}}^{\text{Li(BCC)}}$) and its upper bound represents equilibrium condition 2 ($\mu_{\text{O}}^{\text{Li}_2\text{O}} = \mu_{\text{O}}^{\text{O}_2(\text{g})}$).

addition, our prior study of the Li/Li₃OCl interface also observed that O-termination resulted in a lower energy interface compared to a Cl termination.⁵¹

Table 1 also reports the calculated work of adhesion, W_{ad} , for the crystalline interfaces in both unrelaxed (as calculated by the UBER)^{35–38} and relaxed geometries. The stoichiometric interface exhibits moderate adhesion with unrelaxed and relaxed values of 0.08 and 0.18 J/m², respectively; these energies are comparable to those of the LiF and Li₂CO₃ interfaces in the study of Liu et al. (relaxed energies ranging from 0.065 to 0.167 J/m²).³⁴ On the other hand, the oxygen-rich interface is very strongly adhered, with values more than 30 times larger than those obtained for the stoichiometric interface (unrelaxed and relaxed values of 4.28 and 6.69 J/m²,

respectively). The reason for this appears to be twofold. First, as discussed above, the O-terminated surface interacts very strongly with the Li metal surface, decreasing the value of $\gamma_{\text{Li}/\text{Li}_2\text{O}}$ in eq 8. Second, the O-rich Li₂O(111) surface is higher in energy than the stoichiometric Li₂O(111) surface by roughly 1.0 J/m²,³³ increasing the value of $\sigma_{\text{Li}_2\text{O}}$ in eq 8. Based on these results, Li is predicted to strongly wet a surface with exposed O atoms, resulting in a contact angle approaching 0° for the O-rich surface as compared to 132° for the stoichiometric (Li-terminated) surface.

Charge transfer between the Li and O atoms in the crystalline interface models was analyzed using Voronoi charge partitioning. The Voronoi charges as a function of position normal to the interface are displayed in Figure 4c,d. In the Li₂O portions of the simulation cells, just under 0.3e[−] are transferred from each Li atom to the O atoms, resulting in charges of −0.6 on the oxygens. The systems are roughly charge neutral in the Li metal region of the cells. In both models, the width of the Li/Li₂O interface, as determined by deviations in the charge state of Li atoms from bulk Li and Li₂O, differs from the width of the interfacial region as determined by a visual depiction of the atomic structures (Figure 4a,b). Whereas the atomic structures show an abrupt interface with no overlap of Li and Li₂O regions, based on the charge state of Li atoms, the interfaces extend up to ~3 Å into the Li metal regions.

Figure 4e,f shows the computed shifts in core-level 1s electron binding energies. (Binding energy shifts yield greater accuracy than absolute binding energies; hence, shifts relative to the binding energy in bulk Li were evaluated.) The Li₂O

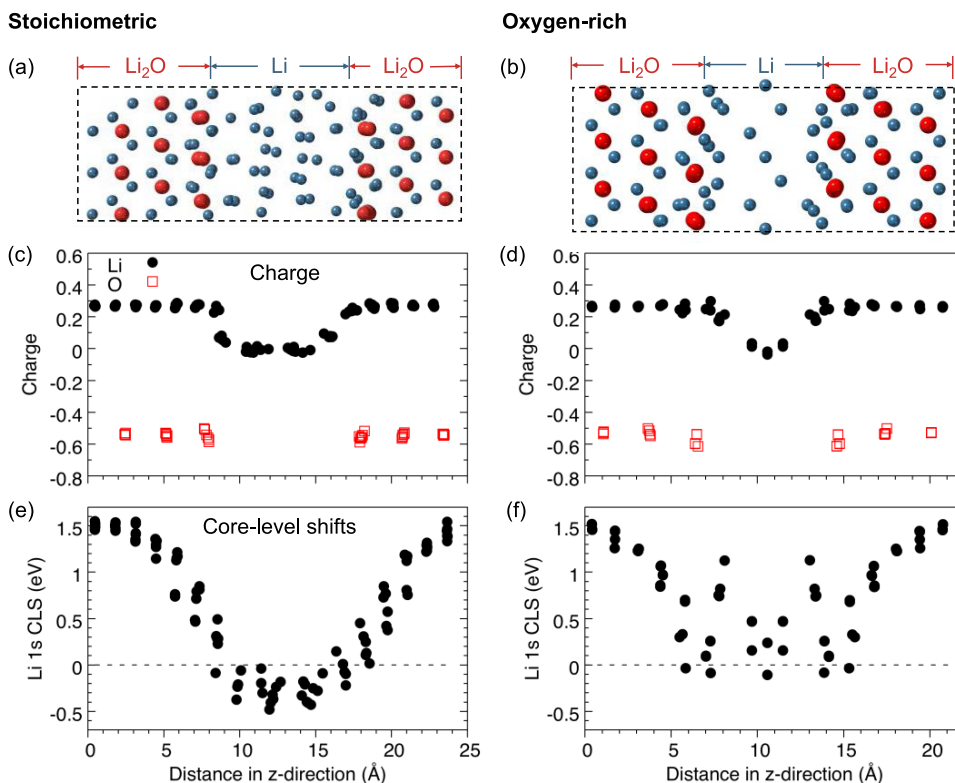


Figure 4. (a) Stoichiometric and (b) oxygen-rich crystalline interface models and corresponding (c, d) Voronoi charges and (e, f) computed shifts in core-level electron binding energies for Li 1s electrons. The charges on Li and O atoms are displayed as black circles and red squares, respectively. Binding energy shifts are displayed with respect to the Li 1s level in bulk Li metal.

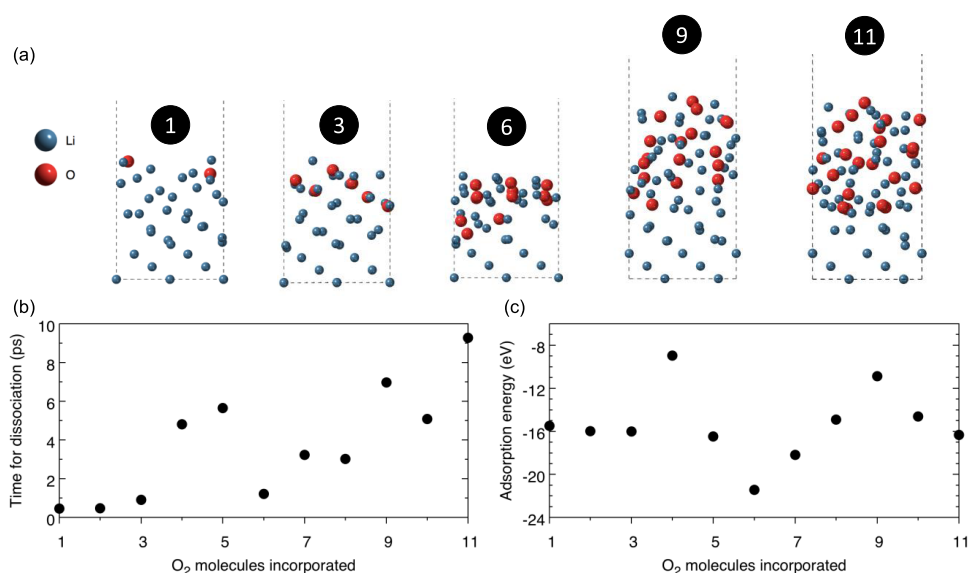


Figure 5. (a) Snapshots displaying the progression of O₂ incorporation into the Li slab (circled numbers give the amount of O₂ molecules incorporated into the slab), (b) simulation time required before each O₂ molecule is dissociated on the Li surface, and (c) adsorption energy progression with O₂ incorporation. Note: the Li slab is enlarged to include five additional Li layers between the incorporation of six and seven O₂ molecules.

portions of the interfaces exhibit shifts that are approximately 1.6–2.0 eV larger than those in the Li metal region. This is expected since Li 1s electrons in Li₂O are more localized than in Li metal, thereby requiring more energy to excite. This effect can be traced to reduced electrostatic repulsion from the Li 2s electrons, which have been transferred to oxygen. Experimentally, the core electron binding energy in Li₂O is about 2.0 eV higher than in Li metal (Figure 1). Considering the experimental standard deviation in these values (>1 eV in Li metal and Li₂O), there is good agreement between the computation and experiment. As with charge transfer, the width of the Li/Li₂O interfacial regions as determined by CLSs is larger than the width of the interfaces based on the atomic structure. Based on the CLSs, the width of the interfaces is roughly 6–9 Å. Consequently, the electronic structure of Li atoms near the interfaces is modified over longer distances than is suggested by the interface structures alone.

Whereas the trends in interfacial charge transfer are similar between the stoichiometric and oxygen-rich interfaces, some differences exist regarding the CLSs for Li. In the oxygen-rich interface, interfacial O atoms interact strongly with some Li atoms in the Li metal region, causing these Li atoms to fill the vacant sites at the interface that would be occupied by Li in stoichiometric Li₂O. A sharp increase is observed in the core-level binding energy for Li at this location, suggesting that these Li atoms exhibit electronic structures that are similar to that of Li in bulk Li₂O.

Amorphous Interface. As described above, the amorphous Li/Li₂O interface was constructed by sequential deposition and incorporation of O₂ molecules on/within a Li surface. All O₂ molecules incorporated into the Li slab underwent dissociation; the time for this dissociation to occur varied as the oxidation progressed. Figure 5a,b shows the amount of simulation time required for each molecule to dissociate during O₂ incorporation. Starting with Figure 5a, it is clear that O atoms readily diffuse into the slab as oxidation proceeds. Newly added O₂ molecules drive existing oxygen atoms deeper into the slab. Furthermore, the amorphous slab

contracts as the number of incorporated O₂ molecules increases. This behavior is expected since Li₂O is denser than Li.

Figure 5b shows that the dissociation time for O₂ roughly increases with increasing oxidation. With increased oxidation, less Li atoms are available at the surface to facilitate the dissociation process. Figure 5c displays the incremental adsorption energy for each O₂ molecule, defined as the energy difference between the current geometry and that of the previous geometry plus an isolated O₂ molecule. The adsorption energy is roughly constant during the oxidation progression, oscillating around a value of about -15 eV/molecule, showing that the thermodynamic preference for O₂ incorporation does not change with increasing oxidation.

Table 1 displays the formation and interfacial energies of the amorphous interface with the thickest oxide layer (22 O atoms). These energies take into account the presence of two vacuum–slab interfaces in the simulation cell by subtracting the surface energies of Li(111) and Li₂O(111) from eqs 2 and 4. The energies in Table 1 are reported for the same set of equilibrium conditions shown for the crystalline interfaces (eqs 6 and 7). Both the formation and interfacial energies of the amorphous interface are lower (i.e., more negative) than those of the crystalline interfaces, signifying that it is the most probable interfacial model.

The pair distribution function (PDF) was computed for the resulting amorphous interface model (containing 11 incorporated O₂ molecules) to analyze its atomic structure (Figure 6). Atoms in the Li metal region of the slab (i.e., where the bottom three Li layers were fixed at their bulk positions) were removed from the slab for this analysis. In addition, the density used in the PDF normalization for the amorphous Li₂O structure was assumed to be decreased by 3.3% relative to the density for crystalline Li₂O as found in our previous work on amorphous Li₂O.⁵² For comparison, the PDF was also computed for crystalline Li₂O at 300 K. These data show that the nearest neighbor Li–O bond distances in the amorphous model roughly align with those in crystalline Li₂O. However,

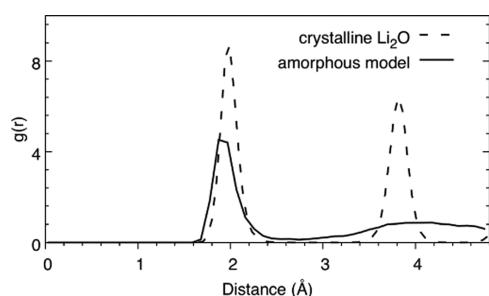


Figure 6. Pair distribution function for Li–O distances in the amorphous interface model (solid line) and in crystalline Li_2O (dashed line).

differences exist in the coordination environment. Integrating the curves in Figure 6 up to the first minimum (~ 2.4 Å), the average coordination number of Li by O atoms in amorphous and crystalline Li_2O are 6 and 8, respectively. Additionally, the second-nearest neighbor bond distance distribution in the amorphous system is much broader and centered 0.3 Å farther than for the equivalent peak in crystalline Li_2O . This suggests that a similar short-range order exists in both amorphous and crystalline Li_2O , whereas the longer range order is less pronounced in the amorphous model, as expected for

disordered materials. A similar analysis was conducted for O–O pairs, and a similar trend was observed.

Figure 7c,d shows the Voronoi charges as a function of oxidation (i.e., number of O_2 molecules added) in the amorphous interface system. Prior to the addition of O_2 , Figure 7c, the charges on the Li slab are roughly zero, in agreement with what is expected for a metallic system. At the completion of the oxidation process, Figure 7d, Li atoms in the portion of the slab exposed to oxygen (right side of the plot) transfer charge to the incorporated O atoms at an amount equivalent to the charge transferred in the crystalline interface in Figure 4 (+0.3 and -0.6 on Li and O atoms, respectively). A transition in the charge state of Li atoms is observed across the region to which O atoms have penetrated. Similar to the crystalline interfaces, the width of this region is ~ 3 Å, and it remains constant as the thickness of the oxide layer increases. As a result, the addition of O_2 molecules (from the standpoint of charge analysis) increases the thickness of the Li_2O layer and not the thickness of the Li/Li $_2\text{O}$ interface. A charge analysis is particularly useful for the amorphous system since it is difficult to discern the extent of the Li/Li $_2\text{O}$ interfacial region from the atomic structure alone (Figure 5a). Of note, in the final oxidized configuration (Figure 7d), the two O atoms positioned at the surface (likely the most recently incorporated

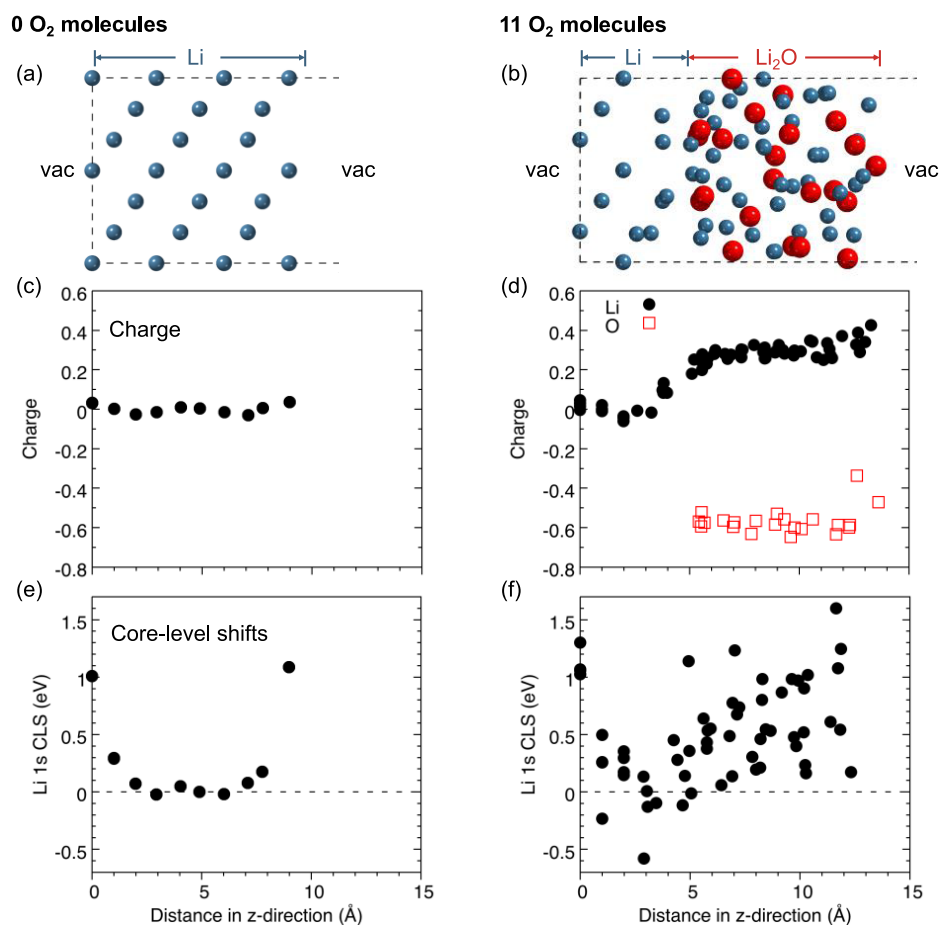


Figure 7. Atomic structures of the amorphous interface model for (a) 0 and (b) 11 O_2 molecules incorporated. The corresponding Voronoi charges for (c) 0 and (d) 11 O_2 molecules incorporated. The charges on Li and O atoms are displayed as black circles and red squares, respectively. Computed shifts in the core-level electron binding energies of Li 1s electrons for (e) 0 and (f) 11 O_2 molecules incorporated. Binding energies are displayed with respect to the Li 1s level in bulk Li metal. The vacuum region used in each simulation cell is denoted on each end of the interface in both models. The gray-shaded box represents the region of the slab to which O_2 molecules are introduced.

O₂ molecule) have each attracted less than the expected 0.6 electrons from the surrounding Li. This finding is in line with the increased time for O₂ dissociation as oxidation progresses (Figure 5c). As the slab becomes more heavily oxidized, the most recently incorporated O₂ molecules must drive existing O₂ molecules deeper into the slab to attract electrons from nearby Li atoms and dissociate.

Figure 7e,f shows the CLSs in the amorphous interface model. With 0 O₂ molecules incorporated (Figure 7e), the electron binding energies in the bulk region of the cell show very good agreement with those of bulk Li metal. Following O₂ incorporation, Figure 7f, the binding energies increase in the portion of the slab exposed to the O₂ molecules. Additionally, the CLSs for some Li atoms shift toward lower binding energies in the bulk portion of the slab. This result reflects a localized fluctuation in electronic energies resulting from the displacement of Li atoms away from their equilibrium positions in Li metal. As with the crystalline interfaces, the width of the Li/Li₂O interface is considerably larger using CLSs as a metric as compared to charge analysis. Nonetheless, in the amorphous model, there is a larger deviation in the CLS values from bulk Li metal and Li₂O, and a clear delineation of Li metal and Li₂O regions of the model is more difficult to identify. This finding is likely due to two factors. First, the overall thickness of the amorphous model (~14 Å) is less than that of the crystalline interfaces (~21–24 Å). Second, there are two free surfaces in the amorphous model simulation cell, and there is a significant surface core-level shift in Li metal (~1 eV), which decreases the portion of the slab displaying bulk Li metal behavior (Figure 7e).

To allow for efficient battery cycling, Li ions must be able to migrate through phases present on the surface of the Li anode with relatively little resistance. To quantify Li-ion transport within the amorphous Li₂O region of the Li/Li₂O interface, the diffusivity of Li⁺ was evaluated at several temperatures using AIMD. Figure 8 shows the mean-squared displacement (MSD) of Li atoms and an Arrhenius plot of the resulting diffusivities. Each point in the Arrhenius plot represents the average diffusivity extracted from three independent AIMD simulations at each temperature; error bars represent the standard deviation in the data.

Figure 8a shows that at shorter times ($\delta t < 0.02$ ps) the MSD is proportional to δt^2 , consistent with expected short-range vibrational motion (i.e., ballistic transport). At longer times ($\delta t > 1$ ps), the MSD is proportional to δt , indicating the presence of long-range diffusional displacements. Importantly, the calculated Li-ion diffusivities in the amorphous Li₂O region of the interface are roughly 3 orders of magnitude larger than those reported in crystalline Li₂O in prior experimental^{53,54} and computational⁵⁵ studies. This behavior mimics the findings of other studies that reported enhanced ionic transport in the amorphous analogues of crystalline materials, such as Li₂O₂⁵² and Li₃PS₄.⁵⁶ Such behavior in disordered materials is often attributed to shallower corrugations of the potential energy surface traversed by migrating ions.⁵⁷ Furthermore, the enhanced Li-ion diffusivities observed here suggest a potential role for the Li/Li₂O interface in promoting Li-ion transport. A recent experimental study of Li transport in thin Li₂O films grown on Li metal also observed Li-ion diffusivities that were several orders of magnitude larger than in bulk Li₂O pellets.⁵⁸

Figure 8b shows that the calculated diffusivity data are well fit by an Arrhenius relationship. From the slope of the fitted

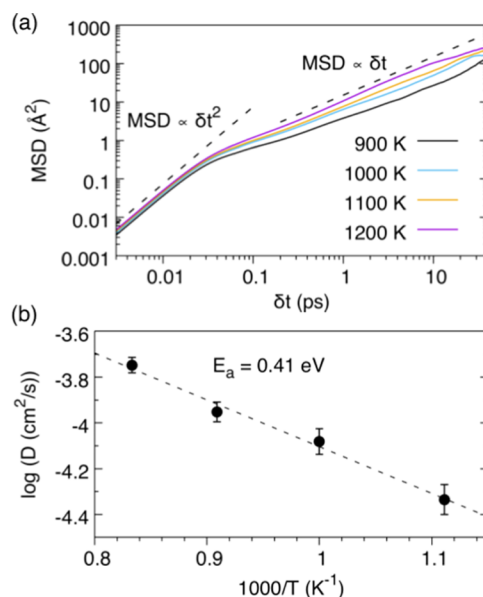


Figure 8. (a) Mean-squared displacement of Li atoms in the amorphous model with 11 O₂ molecules incorporated at 900, 1000, 1100, and 1200 K shown as the black, blue, orange, and purple curves, respectively. The dashed lines designate the limiting behavior at short and long times (i.e., proportionality with respect to δt^2 and δt). (b) Arrhenius plot of Li-ion diffusivities at each temperature as determined from the diffusional displacement regime.

trendline, the activation energy for Li-ion diffusion, E_a , was calculated to be 0.41 eV. For an SEI to be useful, it must allow for facile Li-ion transport through its thickness. Materials in the literature that are considered to be fast Li-ion conductors generally exhibit activation energies in the range 0.11–0.39 eV.^{59–62} Taken together, the relatively low activation energy and the high diffusivity reported here for Li-ion migration in amorphous Li₂O may explain why a functional SEI exists in Li-ion batteries.

As previously mentioned, Li₂O is commonly observed as a component in the inner regions of the SEI; moreover, the inner region of the SEI is generally considered to be amorphous.^{58,63} However, the degree of crystallinity exhibited by this phase can vary.^{5,21} Cryo-TEM on the SEI has shown evidence for the presence of crystalline Li₂O,^{5,21} which has been proposed to be important for the mechanical durability of the SEI. Nonetheless, based on the current study, the transport of Li⁺ within the SEI is predicted to improve in the presence of amorphous Li₂O. Hence, increasing the percentage of amorphous Li₂O (relative to crystalline Li₂O) within the SEI may be desirable.

CONCLUSIONS

Li metal anodes have received a great deal of attention for use in next-generation batteries. A key challenge preventing the implementation of Li metal anodes is the function of the SEI. The SEI should prevent continuous electrochemical reaction with the electrolyte, allow for rapid Li⁺ transport, and suppress dendrite formation. Although the overall composition of the SEI will vary with the electrolyte composition, the native oxide layer, Li₂O, is a common SEI component that is expected to constitute the innermost SEI layer in virtually any battery employing a Li metal anode. Many experimental studies have attributed important cycling behavior of LMBs to the presence

and properties of Li₂O. However, studies that directly probe these properties, and those of the Li/Li₂O interface, are rare.

Here, several interface models for the native oxide layer on Li metal were developed. Subsequently, the properties of the Li metal/lithium oxide interface were analyzed in the context of LMBs. These models account for differing (chemical) terminations and degrees of atomic ordering (i.e., crystalline vs amorphous). For each model, the interfacial energy, formation energy, and strain energies were computed. The amorphous interface exhibits the lowest interfacial formation energy, signifying that it is the most probable model. The work of adhesion was computed for two crystalline interfaces with oxygen-rich (O-terminated) and stoichiometric (Li-terminated) structures in Li₂O. The oxygen-rich model displayed a work of adhesion more than 30 times larger than the stoichiometric model, implying that Li will strongly wet a surface with exposed O atoms.

The electronic structures of the crystalline and amorphous models were characterized with Voronoi charge analysis and shifts in Li 1s core-level electron binding energies. In both analyses, the width of the Li/Li₂O interface was predicted to be larger than the width of the interface as determined by a depiction of the atomic structure. Lastly, an analysis of the Li⁺ diffusion in the amorphous model using AIMD showed that the native oxide layer allows for Li-ion transport at a rate that is 3 orders of magnitude faster than in crystalline Li₂O. Hence, by increasing the percentage of amorphous Li₂O in the SEI it may be possible to improve battery performance. In total, the present analysis of the structural, transport, and mechanical properties of the native oxide layer on Li will assist in the optimization of batteries that employ high-capacity Li metal anodes.

AUTHOR INFORMATION

Corresponding Author

Donald J. Siegel – Mechanical Engineering Department, Materials Science & Engineering, Applied Physics Program, University of Michigan Energy Institute, and Joint Center for Energy Storage Research, University of Michigan, Ann Arbor, Michigan 48109, United States; orcid.org/0000-0001-7913-2513; Phone: +1 (734) 764-4808; Email: djsiege@umich.edu

Author

Jeffrey S. Lowe – Davidson School of Chemical Engineering and Department of Chemistry, Purdue University, West Lafayette, Indiana 47907, United States

Complete contact information is available at: <https://pubs.acs.org/10.1021/acsami.0c12468>

Notes

The authors declare no competing financial interest.

ACKNOWLEDGMENTS

This work was supported as part of the Joint Center for Energy Storage Research (JCESR), an Energy Innovation Hub funded by the U.S. Department of Energy, Office of Science, Basic Energy Sciences.

REFERENCES

(1) Cheng, X.-B.; Zhang, R.; Zhao, C.-Z.; Wei, F.; Zhang, J.-G.; Zhang, Q. A Review of Solid Electrolyte Interphases on Lithium Metal Anode. *Adv. Sci.* **2016**, *3*, No. 1500213.

(2) Camacho-Forero, L. E.; Smith, T. W.; Bertolini, S.; Balbuena, P. B. Reactivity at the Lithium–Metal Anode Surface of Lithium–Sulfur Batteries. *J. Phys. Chem. C* **2015**, *119*, 26828–26839.

(3) Camacho-Forero, L. E.; Balbuena, P. B. Elucidating Electrolyte Decomposition under Electron-Rich Environments at the Lithium–Metal Anode. *Phys. Chem. Chem. Phys.* **2017**, *19*, 30861–30873.

(4) Soto, F. A.; Ma, Y.; Martinez De La Hoz, J. M.; Seminario, J. M.; Balbuena, P. B. Formation and Growth Mechanisms of Solid-Electrolyte Interphase Layers in Rechargeable Batteries. *Chem. Mater.* **2015**, *27*, 7990–8000.

(5) Li, Y.; Li, Y.; Pei, A.; Yan, K.; Sun, Y.; Wu, C.-L.; Joubert, L.-M.; Chin, R.; Koh, A. L.; Yu, Y.; Perrino, J.; Butz, B.; Chu, S.; Cui, Y. Atomic Structure of Sensitive Battery Materials and Interfaces Revealed by Cryo–Electron Microscopy. *Science* **2017**, *358*, 506–510.

(6) Kozen, A. C.; Lin, C.-F.; Zhao, O.; Lee, S. B.; Rubloff, G. W.; Noked, M. Stabilization of Lithium Metal Anodes by Hybrid Artificial Solid Electrolyte Interphase. *Chem. Mater.* **2017**, *29*, 6298–6307.

(7) Cheng, X.-B.; Zhang, R.; Zhao, C.-Z.; Zhang, Q. Toward Safe Lithium Metal Anode in Rechargeable Batteries: A Review. *Chem. Rev.* **2017**, *117*, 10403–10473.

(8) Fan, L.; Zhuang, H. L.; Gao, L.; Lu, Y.; Archer, L. A. Regulating Li Deposition at Artificial Solid Electrolyte Interphases. *J. Mater. Chem. A* **2017**, *5*, 3483–3492.

(9) Wan, G.; Guo, F.; Li, H.; Cao, Y.; Ai, X.; Qian, J.; Li, Y.; Yang, H. Suppression of Dendritic Lithium Growth by in Situ Formation of a Chemically Stable and Mechanically Strong Solid Electrolyte Interphase. *ACS Appl. Mater. Interfaces* **2018**, *10*, 593–601.

(10) Lee, D. J.; Lee, H.; Kim, Y.-J.; Park, J.-K.; Kim, H.-T. Sustainable Redox Mediation for Lithium–Oxygen Batteries by a Composite Protective Layer on the Lithium–Metal Anode. *Adv. Mater.* **2016**, *28*, 857–863.

(11) Sun, H.-H.; Dolocan, A.; Weeks, J. A.; Rodriguez, R.; Heller, A.; Mullins, C. B. In Situ Formation of a Multicomponent Inorganic-Rich SEI Layer Provides a Fast Charging and High Specific Energy Li-Metal Battery. *J. Mater. Chem. A* **2019**, *7*, 17782–17789.

(12) Shi, L.; Xu, A.; Zhao, T. First-Principles Investigations of the Working Mechanism of 2D h-BN as an Interfacial Layer for the Anode of Lithium Metal Batteries. *ACS Appl. Mater. Interfaces* **2017**, *9*, 1987–1994.

(13) Huang, J.-Q.; Zhuang, T.-Z.; Zhang, Q.; Peng, H.-J.; Chen, C.-M.; Wei, F. Permselective Graphene Oxide Membrane for Highly Stable and Anti-Self-Discharge Lithium–Sulfur Batteries. *ACS Nano* **2015**, *9*, 3002–3011.

(14) Kazyak, E.; Wood, K. N.; Dasgupta, N. P. Improved Cycle Life and Stability of Lithium Metal Anodes through Ultrathin Atomic Layer Deposition Surface Treatments. *Chem. Mater.* **2015**, *27*, 6457–6462.

(15) Kozen, A. C.; Lin, C.-F.; Pearse, A. J.; Schroeder, M. A.; Han, X.; Hu, L.; Lee, S. B.; Rubloff, G. W.; Noked, M. Next-Generation Lithium Metal Anode Engineering via Atomic Layer Deposition. *ACS Nano* **2015**, *9*, 5884–5892.

(16) Chen, L.; Connell, J. G.; Nie, A.; Huang, Z.; Zavadil, K. R.; Klavetter, K. C.; Yuan, Y.; Sharifi-Asl, S.; Shahbazian-Yassar, R.; Libera, J. A.; Mane, A. U.; Elam, J. W. Lithium Metal Protected by Atomic Layer Deposition Metal Oxide for High Performance Anodes. *J. Mater. Chem. A* **2017**, *5*, 12297–12309.

(17) Adams, B. D.; Carino, E. V.; Connell, J. G.; Han, K. S.; Cao, R.; Chen, J.; Zheng, J.; Li, Q.; Mueller, K. T.; Henderson, W. A.; Zhang, J. G. Long Term Stability of Li-S Batteries Using High Concentration Lithium Nitrate Electrolytes. *Nano Energy* **2017**, *40*, 607–617.

(18) Ryou, M. H.; Lee, Y. M.; Lee, Y.; Winter, M.; Bieker, P. Mechanical Surface Modification of Lithium Metal: Towards Improved Li Metal Anode Performance by Directed Li Plating. *Adv. Funct. Mater.* **2015**, *25*, 834–841.

(19) Sharafi, A.; Kazyak, E.; Davis, A. L.; Yu, S.; Thompson, T.; Siegel, D. J.; Dasgupta, N. P.; Sakamoto, J. Surface Chemistry Mechanism of Ultra-Low Interfacial Resistance in the Solid-State Electrolyte Li₇La₃Zr₂O₁₂. *Chem. Mater.* **2017**, *29*, 7961–7968.

- (20) Hong, S.-T.; Kim, J.-S.; Lim, S.-J.; Yoon, W. Y. Surface Characterization of Emulsified Lithium Powder Electrode. *Electrochim. Acta* **2004**, *50*, 535–539.
- (21) Liu, Y.; Lin, D.; Li, Y.; Chen, G.; Pei, A.; Nix, O.; Li, Y.; Cui, Y. Solubility-Mediated Sustained Release Enabling Nitrate Additive in Carbonate Electrolytes for Stable Lithium Metal Anode. *Nat. Commun.* **2018**, *9*, No. 3656.
- (22) Tang, C.-Y.; Dillon, S. J. In Situ Scanning Electron Microscopy Characterization of the Mechanism for Li Dendrite Growth. *J. Electrochem. Soc.* **2016**, *163*, A1660–A1665.
- (23) Shiraishi, S.; Kanamura, K.; Takehara, Z. Influence of Initial Surface Condition of Lithium Metal Anodes on Surface Modification with HF. *J. Appl. Electrochem.* **1999**, *29*, 867–879.
- (24) Lepley, N. D.; Holzwarth, N. A. W. Modeling Interfaces between Solids: Application to Li Battery Materials. *Phys. Rev. B* **2015**, *92*, No. 214201.
- (25) Koch, S. L.; Morgan, B. J.; Passerini, S.; Teobaldi, G. Density Functional Theory Screening of Gas-Treatment Strategies for Stabilization of High Energy-Density Lithium Metal Anodes. *J. Power Sources* **2015**, *296*, 150–161.
- (26) Kresse, G.; Furthmüller, J. Efficiency of Ab-Initio Total Energy Calculations for Metals and Semiconductors Using a Plane-Wave Basis Set. *Comput. Mater. Sci.* **1996**, *6*, 15–50.
- (27) Kresse, G.; Furthmüller, J. Efficient Iterative Schemes for Ab Initio Total-Energy Calculations Using a Plane-Wave Basis Set. *Phys. Rev. B* **1996**, *54*, 11169–11186.
- (28) Kresse, G.; Hafner, J. Ab Initio Molecular Dynamics for Liquid Metals. *Phys. Rev. B* **1993**, *47*, 558–561.
- (29) Kresse, G.; Hafner, J. Ab Initio Molecular-Dynamics Simulation of the Liquid-Metal–Amorphous-Semiconductor Transition in Germanium. *Phys. Rev. B* **1994**, *49*, 14251–14269.
- (30) Perdew, J. P.; Burke, K.; Ernzerhof, M. Generalized Gradient Approximation Made Simple. *Phys. Rev. Lett.* **1996**, *77*, 3865–3868.
- (31) Kresse, G.; Joubert, D. From ultrasoft pseudopotentials to the projector augmented-wave method. *Phys. Rev. B* **1999**, *59*, 1758–1775.
- (32) Blöchl, P. E. Projector Augmented-Wave Method. *Phys. Rev. B* **1994**, *50*, 17953–17979.
- (33) Radin, M. D.; Rodriguez, J. F.; Tian, F.; Siegel, D. J. Lithium Peroxide Surfaces Are Metallic, While Lithium Oxide Surfaces Are Not. *J. Am. Chem. Soc.* **2012**, *134*, 1093–1103.
- (34) Liu, Z.; Qi, Y.; Lin, Y. X.; Chen, L.; Lu, P.; Chen, L. Q. Interfacial Study on Solid Electrolyte Interphase at Li Metal Anode: Implication for Li Dendrite Growth. *J. Electrochem. Soc.* **2016**, *163*, A592–A598.
- (35) Adams, J. B.; Hector, L. G., Jr.; Siegel, D. J.; Yu, H.; Zhong, J. Adhesion, Lubrication and Wear on the Atomic Scale. *Surf. Interface Anal.* **2001**, *31*, 619–626.
- (36) Siegel, D.; Hector, L., Jr.; Adams, J. Adhesion, Atomic Structure, and Bonding at the Al(111)/ α -Al₂O₃(0001) Interface: A First Principles Study. *Phys. Rev. B* **2002**, *65*, No. 085415.
- (37) Siegel, D. J.; Hector, L. G., Jr.; Adams, J. B. First-Principles Study of Metal–Carbide/Nitride Adhesion: Al/VC vs. Al/VN. *Acta Mater.* **2002**, *50*, 619–631.
- (38) Siegel, D. J.; Hector, L. G., Jr.; Adams, J. B. Adhesion, Stability, and Bonding at Metal/Metal-Carbide Interfaces: Al/WC. *Surf. Sci.* **2002**, *498*, 321–336.
- (39) Wang, Y.; Liu, Z. K.; Chen, L. Q.; Wolverton, C. First-Principles Calculations of B²⁺-Mg₅Si₆/ α -Al Interfaces. *Acta Mater.* **2007**, *55*, 5934–5947.
- (40) Zhang, W.; Smith, J. R. Stoichiometry and Adhesion of Nb/Al₂O₃. *Phys. Rev. B* **2000**, *61*, 16883–16889.
- (41) Zimmermann, J.; Finnis, M. W.; Ciacchi, L. C. Vacancy Segregation in the Initial Oxidation Stages of the TiN(100) Surface. *J. Chem. Phys.* **2009**, *130*, No. 134714.
- (42) Nosé, S. A Unified Formulation of the Constant Temperature Molecular Dynamics Methods. *J. Chem. Phys.* **1984**, *81*, 511–519.
- (43) Tang, W.; Sanville, E.; Henkelman, G. A Grid-Based Bader Analysis Algorithm without Lattice Bias. *J. Phys.: Condens. Matter* **2009**, *21*, No. 084204.
- (44) Sanville, E.; Kenny, S. D.; Smith, R.; Henkelman, G. Improved Grid-Based Algorithm for Bader Charge Allocation. *J. Comput. Chem.* **2007**, *28*, 899–908.
- (45) Henkelman, G.; Arnaldsson, A.; Jónsson, H. A Fast and Robust Algorithm for Bader Decomposition of Charge Density. *Comput. Mater. Sci.* **2006**, *36*, 354–360.
- (46) Yu, M.; Trinkle, D. R. Accurate and Efficient Algorithm for Bader Charge Integration. *J. Chem. Phys.* **2011**, *134*, No. 064111.
- (47) Zeng, Z.; Ma, X.; Ding, W.; Li, W. First-Principles Calculation of Core-Level Binding Energy Shift in Surface Chemical Processes. *Sci. China: Chem.* **2010**, *53*, 402–410.
- (48) Köhler, L.; Kresse, G. Density Functional Study of CO on Rh(111). *Phys. Rev. B* **2004**, *70*, No. 165405.
- (49) Wood, K. N.; Teeter, G. XPS on Li Battery Related Compounds: Analysis of Inorganic SEI Phases and a Methodology for Charge Correction. *ACS Appl. Energy Mater.* **2018**, *1*, 4493–4504.
- (50) He, X.; Zhu, Y.; Epstein, A.; Mo, Y. Statistical Variances of Diffusional Properties from Ab Initio Molecular Dynamics Simulations. *npj Comput. Mater.* **2018**, *4*, No. 18.
- (51) Kim, K.; Siegel, D. J. Predicting Wettability and the Electrochemical Window of Lithium-Metal/Solid Electrolyte Interfaces. *ACS Appl. Mater. Interfaces* **2019**, *11*, 39940–39950.
- (52) Tian, F.; Radin, M. D.; Siegel, D. J. Enhanced Charge Transport in Amorphous Li₂O₂. *Chem. Mater.* **2014**, *26*, 2952–2959.
- (53) Oishi, Y.; Kamei, Y.; Akiyama, M.; Yanagi, T. Self-Diffusion Coefficient of Lithium in Lithium Oxide. *J. Nucl. Mater.* **1979**, *87*, 341–344.
- (54) Akiyama, M.; Ando, K.; Oishi, Y. Self-Diffusion of Constituent Ions in Antifluorite-Cubic Lithium Oxide. *Solid State Ionics* **1981**, *3–4*, 469–472.
- (55) Mulliner, A. D.; Aeberhard, P. C.; Battle, P. D.; David, W. I. F.; Refson, K. Diffusion in Li₂O Studied by Non-Equilibrium Molecular Dynamics for 873 < T/K < 1603. *Phys. Chem. Chem. Phys.* **2015**, *17*, 21470–21475.
- (56) Smith, J. G.; Siegel, D. J. Low-Temperature Paddlewheel Effect in Glassy Solid Electrolytes. *Nat. Commun.* **2020**, *11*, No. 1483.
- (57) Chandra, A.; Bhatt, A.; Chandra, A. Ion Conduction in Superionic Glassy Electrolytes: An Overview. *J. Mater. Sci. Technol.* **2013**, *29*, 193–208.
- (58) Guo, R.; Gallant, B. M. Li₂O Solid Electrolyte Interphase: Probing Transport Properties at the Chemical Potential of Lithium. *Chem. Mater.* **2020**, *32*, 5525–5533.
- (59) Kamaya, N.; Homma, K.; Yamakawa, Y.; Hirayama, M.; Kanno, R.; Yonemura, M.; Kamiyama, T.; Kato, Y.; Hama, S.; Kawamoto, K.; Mitsui, A. A Lithium Superionic Conductor. *Nat. Mater.* **2011**, *10*, 682–686.
- (60) Murugan, R.; Thangadurai, V.; Weppner, W. Fast Lithium Ion Conduction in Garnet-Type Li₇La₃Zr₂O₁₂. *Angew. Chem., Int. Ed.* **2007**, *46*, 7778–7781.
- (61) Dietrich, C.; Weber, D. A.; Sedlmaier, S. J.; Indris, S.; Culver, S. P.; Walter, D.; Janek, J.; Zeier, W. G. Lithium Ion Conductivity in Li₂S–P₂S₅ Glasses – Building Units and Local Structure Evolution during the Crystallization of Superionic Conductors Li₃PS₄, Li₇P₃S₁₁ and Li₄P₂S₇. *J. Mater. Chem. A* **2017**, *5*, 18111–18119.
- (62) Rayavarapu, P. R.; Sharma, N.; Peterson, V. K.; Adams, S. Variation in Structure and Li⁺-Ion Migration in Argyrodite-Type Li₆PSSX (X = Cl, Br, I) Solid Electrolytes. *J. Solid State Electrochem.* **2012**, *16*, 1807–1813.
- (63) Wang, A.; Kadam, S.; Li, H.; Shi, S.; Qi, Y. Review on Modeling of the Anode Solid Electrolyte Interphase (SEI) for Lithium-Ion Batteries. *npj Comput. Mater.* **2018**, *4*, No. 15.
- (64) Povey, A. F.; Sherwood, P. M. A. Covalent Character of Lithium Compounds Studied by X-Ray Photoelectron Spectroscopy. *J. Chem. Soc., Faraday Trans. 2* **1974**, *70*, 1240–1246.
- (65) Contour, J. P.; Salesse, A.; Froment, M.; Garreau, M.; Thevenin, J.; Warin, D. Analysis by electron microscopy and

photoelectron spectroscopy of lithium surfaces polarized in anhydrous organic electrolytes. *J. Microsc. Spectrosc. Electroniques* **1979**, *4*, 483.

(66) Suo, L.; Hu, Y.-S.; Li, H.; Armand, M.; Chen, L. A New Class of Solvent-in-Salt Electrolyte for High-Energy Rechargeable Metallic Lithium Batteries. *Nat. Commun.* **2013**, *4*, No. 1481.

(67) Yao, K. P. C.; Kwabi, D. G.; Quinlan, R. A.; Mansour, A. N.; Grimaud, A.; Lee, Y.-L.; Lu, Y.-C.; Shao-Horn, Y. Thermal Stability of Li₂O₂ and Li₂O for Li-Air Batteries: In Situ XRD and XPS Studies. *J. Electrochem. Soc.* **2013**, *160*, A824–A831.

(68) Ota, H.; Sakata, Y.; Wang, X.; Sasahara, J.; Yasukawa, E. Characterization of Lithium Electrode in Lithium Imides/Ethylene Carbonate and Cyclic Ether Electrolytes. *J. Electrochem. Soc.* **2004**, *151*, A437–A446.

(69) Lu, Y.-C.; Crumlin, E. J.; Veith, G. M.; Harding, J. R.; Mutoro, E.; Baggetto, L.; Dudney, N. J.; Liu, Z.; Shao-Horn, Y. In Situ Ambient Pressure X-Ray Photoelectron Spectroscopy Studies of Lithium-Oxygen Redox Reactions. *Sci. Rep.* **2012**, *2*, No. 715.

(70) Yen, S. P. S.; Shen, D.; Vasquez, R. P.; Grunthner, F. J.; Somoano, R. B. Chemical and Morphological Characteristics of Lithium Electrode Surfaces. *J. Electrochem. Soc.* **1981**, *128*, 1434–1438.

(71) Mallinson, C. F.; Castle, J. E.; Watts, J. F. Analysis of the Li KLL Auger Transition on Freshly Exposed Lithium and Lithium Surface Oxide by AES. *Surf. Sci. Spectra* **2013**, *20*, 113–127.

(72) Aurbach, D.; Pollak, E.; Elazari, R.; Salitra, G.; Kelley, C. S.; Affinito, J. On the Surface Chemical Aspects of Very High Energy Density, Rechargeable Li–Sulfur Batteries. *J. Electrochem. Soc.* **2009**, *156*, A694–A702.

(73) Wu, Q.-H.; Thissen, A.; Jaegermann, W. Photoelectron Spectroscopic Study of Li Oxides on Li Over-Deposited V₂O₅ Thin Film Surfaces. *Appl. Surf. Sci.* **2005**, *250*, 57–62.

(74) Marino, C.; Darwiche, A.; Dupré, N.; Wilhelm, H. A.; Lestriez, B.; Martinez, H.; Dedryvère, R.; Zhang, W.; Ghamouss, F.; Lemordant, D.; Monconduit, L. Study of the Electrode/Electrolyte Interface on Cycling of a Conversion Type Electrode Material in Li Batteries. *J. Phys. Chem. C* **2013**, *117*, 19302–19313.

(75) Wagner, C. D.; Muilenberg, G. E. *Handbook of X-ray Photoelectron Spectroscopy: A Reference Book of Standard Data for Use in X-ray Photoelectron Spectroscopy*; PerkinElmer Corporation, 1979.

(76) Surface State Analysis without Exposure to Atmosphere “XPS, AES”. <http://www.jfe-tec.co.jp/en/battery/case/09.html> (accessed Oct 17, 2018).

(77) An, S. J.; Li, J.; Sheng, Y.; Daniel, C.; Wood, D. L. Long-Term Lithium-Ion Battery Performance Improvement via Ultraviolet Light Treatment of the Graphite Anode. *J. Electrochem. Soc.* **2016**, *163*, A2866–A2875.

(78) Ismail, I.; Noda, A.; Nishimoto, A.; Watanabe, M. XPS Study of Lithium Surface after Contact with Lithium-Salt Doped Polymer Electrolytes. *Electrochim. Acta* **2001**, *46*, 1595–1603.

(79) Cheng, L.; Crumlin, E. J.; Chen, W.; Qiao, R.; Hou, H.; Franz Lux, S.; Zorba, V.; Russo, R.; Kostecki, R.; Liu, Z.; Persson, K.; Yang, W.; Cabana, J.; Richardson, T.; Chen, G.; Doeff, M. The Origin of High Electrolyte–Electrode Interfacial Resistances in Lithium Cells Containing Garnet Type Solid Electrolytes. *Phys. Chem. Chem. Phys.* **2014**, *16*, 18294–18300.

(80) Kanamura, K.; Tamura, H.; Takehara, Z. XPS Analysis of a Lithium Surface Immersed in Propylene Carbonate Solution Containing Various Salts. *J. Electroanal. Chem.* **1992**, *333*, 127–142.

(81) Dedryvère, R.; Gireaud, L.; Grugeon, S.; Laruelle, S.; Tarascon, J.-M.; Gonbeau, D. Characterization of Lithium Alkyl Carbonates by X-ray Photoelectron Spectroscopy: Experimental and Theoretical Study. *J. Phys. Chem. B* **2005**, *109*, 15868–15875.

(82) Kanamura, K.; Tamura, H.; Shiraishi, S.; Takehara, Z.-I. XPS Analysis for the Lithium Surface Immersed in γ -Butyrolactone Containing Various Salts. *Electrochim. Acta* **1995**, *40*, 913–921.

(83) Shchukarev, A.; Korolkov, D. XPS Study of Group IA Carbonates. *Open Chem.* **2004**, *2*, 347–362.